Supporting Information for:

A Kinetic Study of Mechanochemical Halogen Bond Formation by *In-situ* ^{31}P Solid-State NMR Spectroscopy

Yijue Xu,[‡] Lysiane Champion,[‡,£] Bulat Gabidullin,[‡] and David L. Bryce[‡,*]

[‡]Department of Chemistry and Biomolecular Sciences
University of Ottawa
10 Marie Curie Private
Ottawa, Ontario K1N 6N5
Canada

*Author to whom correspondence is to be addressed
Tel: +1-613-562-5800 ext.2018; fax: +613-562-5170
Email: dbryce@uottawa.ca

[£] Université de Poitiers, Faculté des Sciences Fondamentales et Appliquées, 40 avenue du Recteur Pineau, 86022 Poitiers cedex, France

EXPERIMENTAL

Sample Preparation

Triphenylphosphine oxide (Ph_3PO) and *para*-diiodotetrafluorobenzene (p-$C_6F_4I_2$) were purchased from Sigma Aldrich. p-$C_6F_4I_2$ was used without any further purification, but Ph_3PO was recrystallised from acetone to give the pure monoclinic polymorph. Equimolar amounts of these two starting materials were dissolved into a minimum volume of acetonitrile. Slow evaporation from acetonitrile at room temperature produced a pure crystal of **1**, and evaporation by boiling acetonitrile gave a crystal of **2**. The procedure to set up for an *in-situ* SSNMR experiment is adapted from previous literature.[1] The two starting materials were pre-ground into fine powders separately using a mortar and pestle. To initiate the reaction, 0.0661 g of pre-ground Ph_3PO was gently mixed with 0.0955 g of pre-ground p-$C_6F_4I_2$ followed immediately by the addition at time $t = 0$ of different volumes of acetonitrile (5 μL for temperature and spinning speed studies; and 0, 3, and 4 μL for liquid effect studies). The mixture was immediately vortexed for 10 seconds at top speed using a benchtop vortexer. Then the mixture of powders was immediately packed into a 4 mm o.d. zirconia rotor followed by normal sample spinning and NMR data acquisition. There was a 20 to 30 minute gap (t_0) between the initiation of the co-crystallization and the end of the acquisition of the first NMR spectrum.

In-situ ^{31}P Solid-State NMR Spectroscopy

Data were acquired with a 9.4 T magnet, Bruker AVANCE III console, and a 4 mm Bruker HXY probe (University of Ottawa, Ottawa, Canada). ^{31}P chemical shifts were referenced to ammonium dihydrogen phosphate ($\delta_{iso} = 0.81$ ppm with respect to 85% H_3PO_4). A standard cross-polarization pulse sequence was employed. The $\pi/2$ pulse length and contact time were 3.4 μs and 2 ms, respectively. The recycle delay was set to be 2 minutes and the number of scan was 8 for each spectrum. The sample temperature for all the experiments was calibrated using the ^{207}Pb resonance of lead nitrate.[2] The temperature was held constant where required by heating and cooling regulated by an FTS Systems TC-84 temperature controller. In order to study the effect of temperature on the reaction, a series of *in-situ* ^{31}P CP/MAS experiments was performed at temperatures of 15, 25, and 35 ℃ at a spinning frequency of 10 kHz. In order to investigate the effect of pressure produced by MAS, experiments were carried out at constant temperature (25 ℃) and various MAS rates (8, 10, and 12 kHz). To observe the effect of different amounts of acetonitrile added, the reaction was started by adding 0, 3 (24 mol%), or 4 (32 mol%) μL of liquid and then monitored at 45 ℃ at a 10 kHz spinning speed. The relative CP efficiencies of different compounds were measured. Exactly 0.0850 g starting material (monoclinic Ph_3PO), 0.1571 g compound **1,** and 0.0981 g **2** were packed separately into three different 4 mm o.d. zirconia rotors. The ^{31}P CP/MAS NMR spectra of three compounds were recorded using the same data collection parameters. The resulting isotropic peak integrals were measured to compare the different CP efficiencies.

Powder X-ray Diffraction

All PXRD patterns were obtained using a Rigaku Ultima IV powder diffractometer at room temperature (298 ± 1 K) with a copper source and one diffracted beam monochromator from 5° to 50° (2θ range) in increments of 0.02° with a scan rate of 1° per minute. Simulations were generated using Mercury 3.8 software from the Crystallographic Data Center.

CASTEP Calculations

The ^{31}P magnetic shielding tensors were calculated using CASTEP software version 4.4[3] on the Wooki cluster at the University of Ottawa. The input file generated from Materials Studio v. 4.4 (Accelrys) used the generalized gradient approximation (GGA) with the functional of

Perdew, Burke, Ernzerhof (PBE)[4] and "on-the-fly" pseudopotentials to perform the geometry optimization of the hydrogen positions followed by NMR calculation. The cut-off energy of 610.0 eV and the *k*-point grid of 2×1×1 were used. Gauge-including projector-augmented wave density functional theory (GIPAW DFT)[5] calculations were applied to calculate all the NMR parameters, which were extracted from the CASTEP NMR output file using EFGShield version 4.2[6].

Single-crystal X-ray diffraction

The crystal of **2** was mounted on a thin glass fiber using paraffin oil. Prior to data collection the crystal was cooled to 200 ± 2 K. Data were collected on Bruker AXS single crystal diffractometer equipped with a sealed Mo tube source (wavelength 0.71073 Å) and APEX II CCD detector. Raw data collection and processing were performed with the Bruker APEX II software package.[7] Semi-empirical absorption corrections based on equivalent reflections were applied.[8] Systematic absences in the diffraction dataset and unit cell parameters were consistent with the triclinic *P*-1 (#2) space group. The structure was solved by direct methods and refined with a full-matrix least-squares procedure based on F^2, using SHELXL[9] and WinGX[10]. All non-hydrogen atoms were refined anisotropically. The positions of hydrogen atoms were calculated based on the geometry of related non-hydrogen atoms.

The compound crystallizes with 3 Ph_3PO and 2.5 *p*-$C_6F_4I_2$ molecules in the asymmetric unit. One of the *p*-$C_6F_4I_2$ molecules lies on an inversion centre. No additional restraints or constraints were applied during the refinement.

Table S1. Crystallographic Data and Selected Data Collection Parameters for **2**

Empirical formula	**$C_{69}H_{45}F_{10}I_5O_3P_3$**
Formula weight	1839.46
Crystal size, mm^3	0.955 x 0.786 x 0.548
Crystal system	triclinic
Space group	$P\bar{1}$
Z	2
***a*, Å**	8.4755(8)
***b*, Å**	18.6290(18)
***c*, Å**	21.907(2)
α, °	82.080(1)
β, °	78.944(1)
γ, °	80.992(1)
Volume, Å^3	3332.1(6)
Calculated density, Mg m^{-3}	1.833
Absorption coefficient, mm^{-1}	2.480
***F*(000)**	1766
θ range for data collection, °	2.098 to 28.213
Limiting indices	$-11 \leq h \leq 10$, $-24 \leq k \leq 24$, $-29 \leq l \leq 28$
Reflections collected/ unique	39918 / 15885
R_{int}	0.0231
Completeness to θ = 25.242°, %	99.6
Max and min transmission	0.7457 and 0.4061
Data/ restraints/ parameters	15885 / 0 / 811
Goodness-of-fit on F^2	1.076
Final *R* indices [$I > 2\alpha(I)$]	$R_1 = 0.0261$, $wR_2 = 0.0609$
***R* indices (all data)**	$R_1 = 0.0311$, $wR_2 = 0.0632$
largest diff. peak and hole, e·Å^{-3}	0.699 and -1.332

Table S2. Compound Numbering and Local Halogen Bonding Geometrical Information from Single-Crystal X-ray Diffraction

Compound	P site	#I	$d_{\mathrm{I}\ldots\mathrm{O}}$/Å	$d_{\mathrm{P=O}}$/Å	R_{XB}[a]	$\theta_{\mathrm{O}\ldots\mathrm{I\text{-}C}}$/deg	$\theta_{\mathrm{P=O}\ldots\mathrm{I}}$/deg	$\theta_{\mathrm{I..O}\ldots\mathrm{I}}$/deg
1[b]		1	2.725	1.495	0.779	175.7	152.1	
2	**2_1**	1	2.766	1.493	0.790	172.4	136.5	81.4
	2_1	2a	3.304	1.493	0.944	160.3	140.4	
	2_3	2b	2.856	1.491	0.816	175.6	142.3	
	2_2	3	2.759	1.496	0.788	176.6	132.8	

[a] R_{XB} is the normalized distance parameter, $R_{XB} = d_{I\cdots O}/\sum d_{VDW}$, where $d_{\mathrm{I}\ldots\mathrm{O}}$ is the shortest distance between the oxygen and iodine and $\sum d_{VDW}$ is the sum of their van der Waals radii (1.52 Å for O and 1.98 Å for I).

[b] Contains one extra *p*-$C_6F_4I_2$, which is not involved in halogen bonding. The crystallographic information for **1** has been reported previously.[11]

Table S3. Solid-State Rate and Integral Expressions for 12 Different Reaction Models[a]

Model	Differential Form $f(\alpha) = 1/k \frac{d\alpha}{dt'}$	Integral Form $g(\alpha) = kt'$	Avrami Exponent n[b]
	Nucleation Models		
Avrami-Erofeyev (A2)	$2(1-\alpha)[-\ln(1-\alpha)]^{1/2}$	$[-\ln(1-\alpha)]^{1/2}$	2
Avrami-Erofeyev (A3)	$3(1-\alpha)[-\ln(1-\alpha)]^{2/3}$	$[-\ln(1-\alpha)]^{1/3}$	3
Avrami-Erofeyev (A4)	$4(1-\alpha)[-\ln(1-\alpha)]^{3/4}$	$[-\ln(1-\alpha)]^{1/4}$	4
	Geometrical contraction Models		
Contracting Area (R2)	$2(1-\alpha)^{1/2}$	$1-(1-\alpha)^{1/2}$	1.11
Contracting Volume (R3)	$3(1-\alpha)^{2/3}$	$1-(1-\alpha)^{1/3}$	1.07
	Diffusion Models		
One Dimensional Diffusion (D1)	$1/(2\alpha)$	α^2	0.62
Two Dimensional Diffusion (D2)	$-[1/\ln(1-\alpha)]$	$(1-\alpha)\ln(1-\alpha)+\alpha$	0.57
Three Dimensional Diffusion (D3)	$[3(1-\alpha)^{2/3}]/\{2[1-(1-\alpha)^{1/3}]\}$	$[1-(1-\alpha)^{1/3}]^2$	0.54
Ginstling-Brounshtein (D4)	$3/\{2[(1-\alpha)^{-1/3}-1]\}$	$1-(\frac{2}{3})\alpha-(1-\alpha)^{2/3}$	0.57
	Reaction Order Models		
First-Order (F1)	$(1-\alpha)$	$-\ln(1-\alpha)$	1
Second-Order (F2)	$(1-\alpha)^2$	$1/(1-\alpha)-1$	
Third-Order (F3)	$(1-\alpha)^3$	$(1/2)[(1-\alpha)^{-2}-1]$	

[a] The table is adapted from reference 12.

[b] *n* values for the partial models are obtained from reference 13.

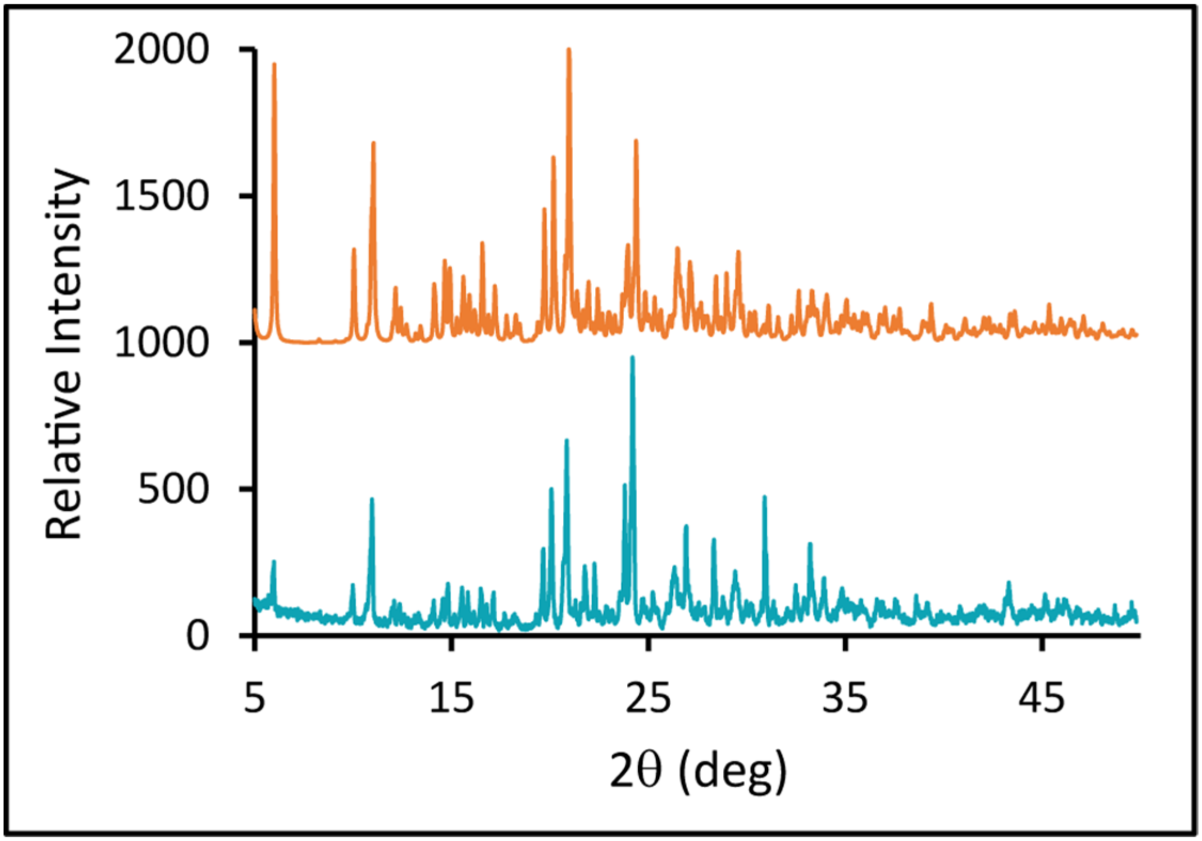

Figure S1. Experimental powder X-ray diffraction pattern (shown in turquoise) for halogen-bonded co-crystal **2**. All data were acquired using a Rigaku Ultima IV diffractometer with 2θ ranging from 5º to 50º at a rate of 1º per minute. The calculated powder X-ray diffraction pattern from the single crystal structure data is presented in orange at the top. Simulations were generated using Mercury 3.8 software from the Crystallographic Data Center.

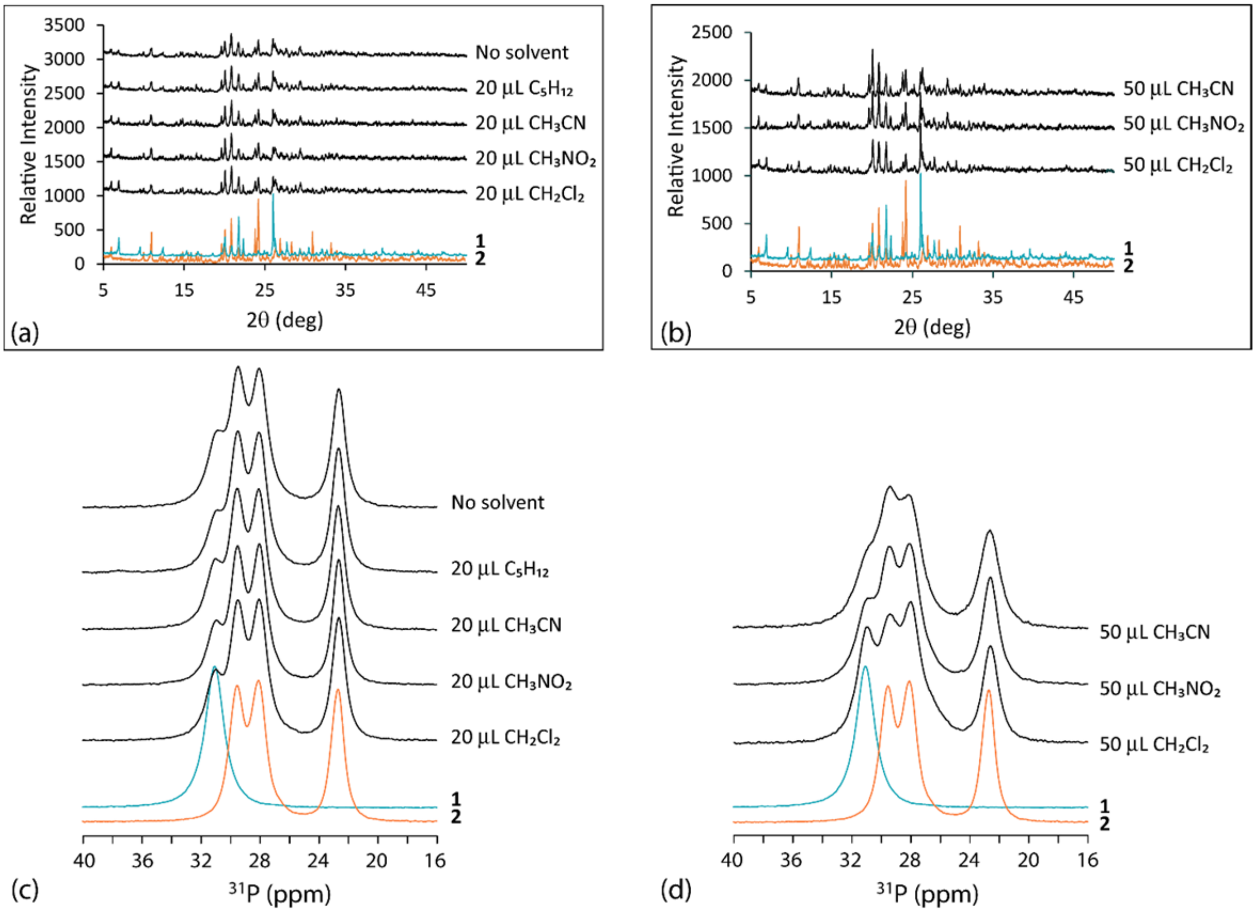

Figure S2. Experimental powder X-ray diffraction patterns for the final product (black) from ball milling with 20 µL (a) and 50 µL (b) of different liquids at 30 Hz for 1 h and halogen-bonded cocrystals from slow evaporation: **1** (turquoise) and **2** (orange). The MAS spinning speed for the ball milled product is 8 kHz and for the halogen-bonded cocrystals from slow evaporation is 10 kHz. Here, mechanochemical synthesis of **1** was attempted by ball milling equimolar amounts of Ph_3PO and *p*-$C_6F_4I_2$ with different liquids at 30 Hz in 25 mL stainless steel milling jars for 1 h. However, as shown in PXRD and ^{31}P CP/MAS spectra, the final product was consistently a mixture of **1** and **2**.

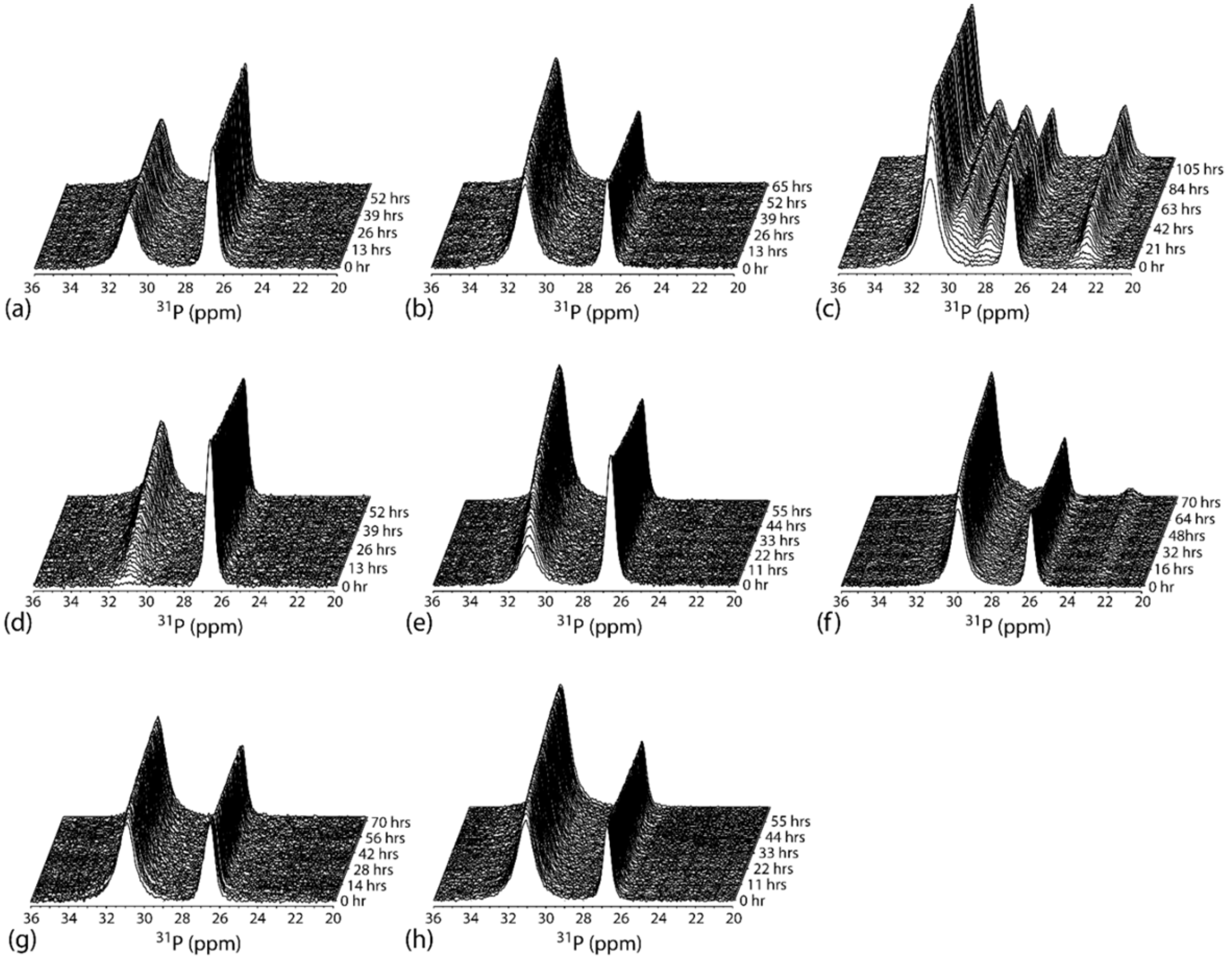

Figure S3. *In-situ* ^{31}P CP/MAS SSNMR spectra of the reacting Ph_3PO and *p*-$C_6F_4I_2$ obtained at 9.4 T under different conditions: (a) at 15 ℃ with a 10 kHz spinning speed and an addition of 5 μL acetonitrile, (b) at 25 ℃ with a 10 kHz spinning speed and an addition of 5 μL acetonitrile, (c) at 35 ℃ with a 10 kHz spinning speed and an addition of 5 μL acetonitrile, (d) at 45 ℃ with a 10 kHz spinning speed and no liquid, (e) at 45 ℃ with a 10 kHz spinning speed and an addition of 3 μL acetonitrile, and (f) at 45 ℃ with a 10 kHz spinning speed and an addition of 4 μL acetonitrile, (g) at 25 ℃ with a 8 kHz spinning speed and an addition of 5 μL acetonitrile, (h) at 25 ℃ with a 12 kHz spinning speed and an addition of 5 μL acetonitrile. Each spectrum was collected for 16 min (8 scans, 2 min recycle delay). Only the isotropic peaks are shown here.

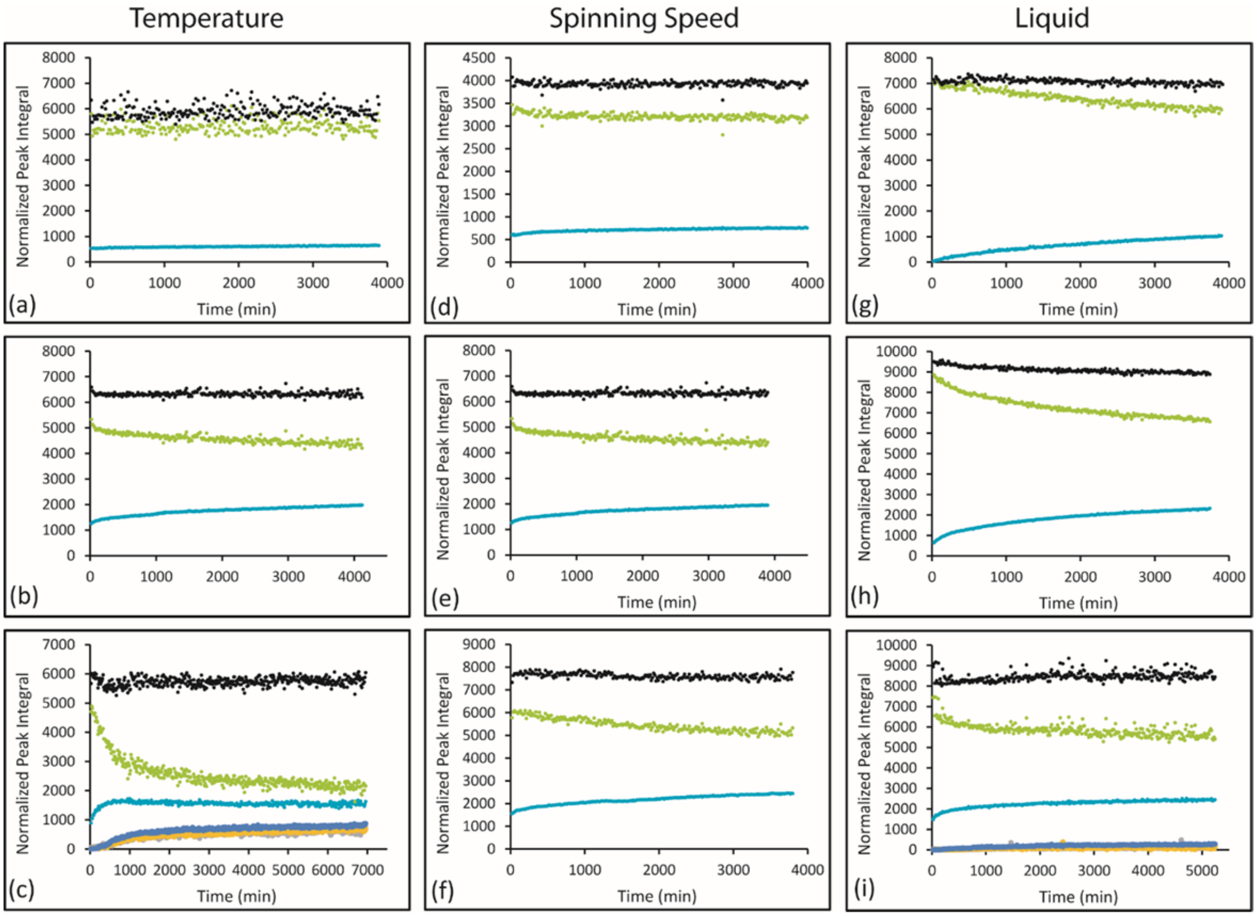

Figure S4. Time-resolved changes in the normalized peak integrals for the isotropic peaks of the starting material Ph_3PO (δ_{iso} = 26.6 ppm) shown in green, halogen-bonded cocrystal **1** (δ_{iso} = 30.7 ppm) shown in turquoise and **2** (δ_{iso} = 22.7 ppm, δ_{iso} = 28.1 ppm, and δ_{iso} = 29.6 ppm) shown in blue, yellow, and grey, respectively under different conditions: (a) at 15 °C with a 10 kHz spinning speed and an addition of 5 μL acetonitrile, (b) at 25 °C with a 10 kHz spinning speed and an addition of 5 μL acetonitrile, (c) at 35 °C with a 10 kHz spinning speed and an addition of 5 μL acetonitrile, (d) at 25 °C with a 8 kHz spinning speed and an addition of 5 μL acetonitrile, (e) at 25 °C with a 10 kHz spinning speed and an addition of 5 μL acetonitrile, (f) at 25 °C with a 12 kHz spinning speed and an addition of 5 μL acetonitrile, (g) at 45 °C with a 10 kHz spinning speed and no liquid, (h) at 45 °C with a 10 kHz spinning speed and an addition of 3 μL acetonitrile, and (i) at 45 °C with a 10 kHz spinning speed and an addition of 4 μL acetonitrile. The sum of all the peak integrals (black) remains constant, indicating the absence of amorphous intermediate.

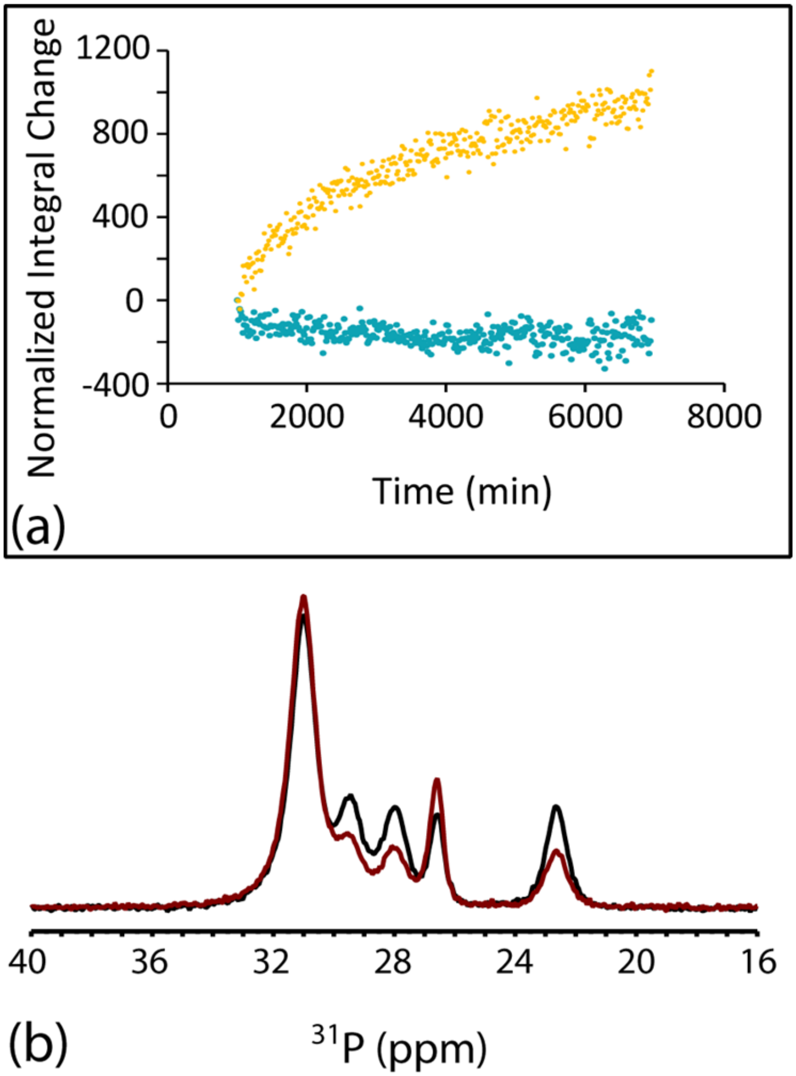

Figure S5. (a) Normalized peak integral change ($I_t - I_{t=16.5h}$) of **1** (turquoise) and the sum of three peaks in **2** (yellow) after around 16.5 h. The more significant increase for **2** indicates that the formation of **2** is mainly but not exclusively from direct cocrystallisation between the two starting materials. (b) Comparison between the experimental ^{31}P CP/MAS SSNMR spectra of the mixture at t = 16.5 h (red) and the mixture at the end time point (black). The slight decrease in peak intensity of **1** (at ~31 ppm) further indicates the conversion of some **1** to **2**.

The Kinetic Analysis of Formation of 1

There is not necessarily a universal crystallisation mechanism for the cocrystallisation process. Even for the same starting materials, different mechanism may prevail depending on the reaction conditions. Previous literature cited in the main text shows that the interpretation of n values can be challenging and the exact mechanism cannot always be determined unequivocally only from kinetics. However, here the $n < 1$ values for the formation of **1** reveal that the reaction mechanism is mainly diffusion-controlled and that the rate of nucleation plays a less significant role or even no role ($n \sim 0.5$) in determining the reaction rate. The best fits to the theoretical kinetic models were obtained with the one dimensional diffusion (D1) model, which is also supported by n values (0.64 ~ 0.85) that can be used to infer information about the mechanism of crystallisation from reference 13. When 4 μL CH_3CN was added initially, both better fits with the D2 and D4 models and the smaller n (0.57 ± 0.01) value indicate that the diffusion mechanism shifts from lower dimension (D1) to higher dimension (D2 or D4). Note that the data points recorded after the initial appearance of **2** are excluded from the kinetic analysis of **1** because the latter then undergoes two processes: formation from the cocrystallisation process and consumption from conversion to **2**.

Limitations in Accuracy and Precision of the Activation Energy

The large error on the reported activation energy follows from the linear regression algorithm used to fit the somewhat non-linear data. Limitations in the accuracy and precision of the value of the activation energy may arise from several factors. Two of the important factors presently are:

- possible inherently non-linear (non-Arrhenius) behavior of the reaction, meaning that fitting the data with a straight line necessarily results in significant error;
- possible non-uniform particle size distribution (Our particles were prepared by simple grinding with a mortar and pestle, and the same batch was used for all experiments; however, there is likely a distribution of particle sizes (μm scale). Particle size was not investigated as a variable in this work, but we fully expect that the kinetics of the reaction may change as the particle size, and thus surface area, is changed).

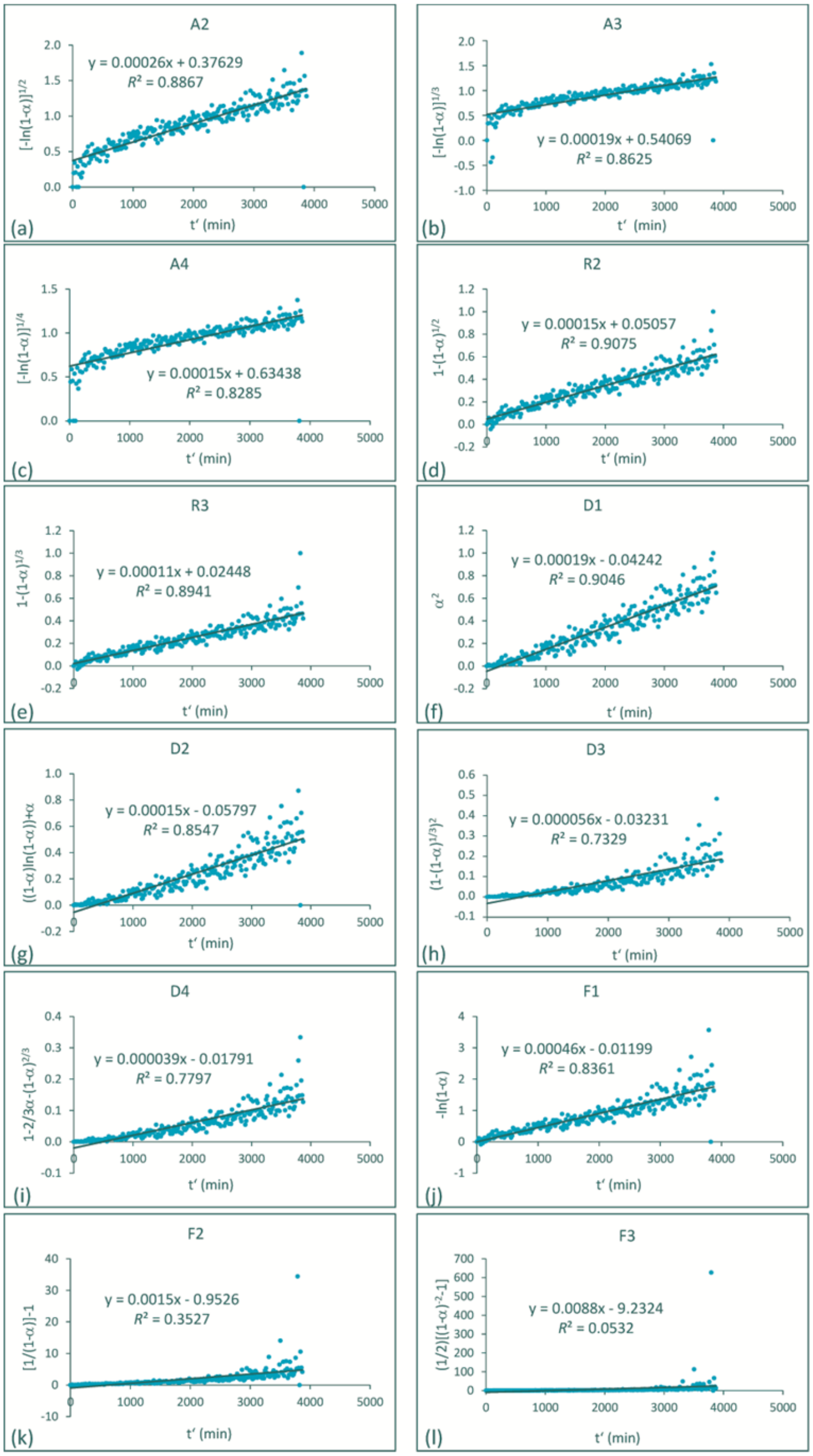

Figure S6. The fitting of conversion fraction α for the MAS *in-situ* formation of **1** (15 ℃, 10 kHz MAS, 5 μL acetonitrile), after linearization α to 12 different models of solid-state reactivity: (a) the A2 model; (b) the A3 model; (c) the A4 model (d) the R2 model; (e) the R3 model; (f) the D1 model; (g) the D2 model; (h) the D3 model; (i) the D4 model; (j) the F1 model; (k) the F2 model; (l) the F3 model. The integrated rate functions, $g(\alpha)$, varying for the different models, are given on the y-axis and also summarized in Table S3.

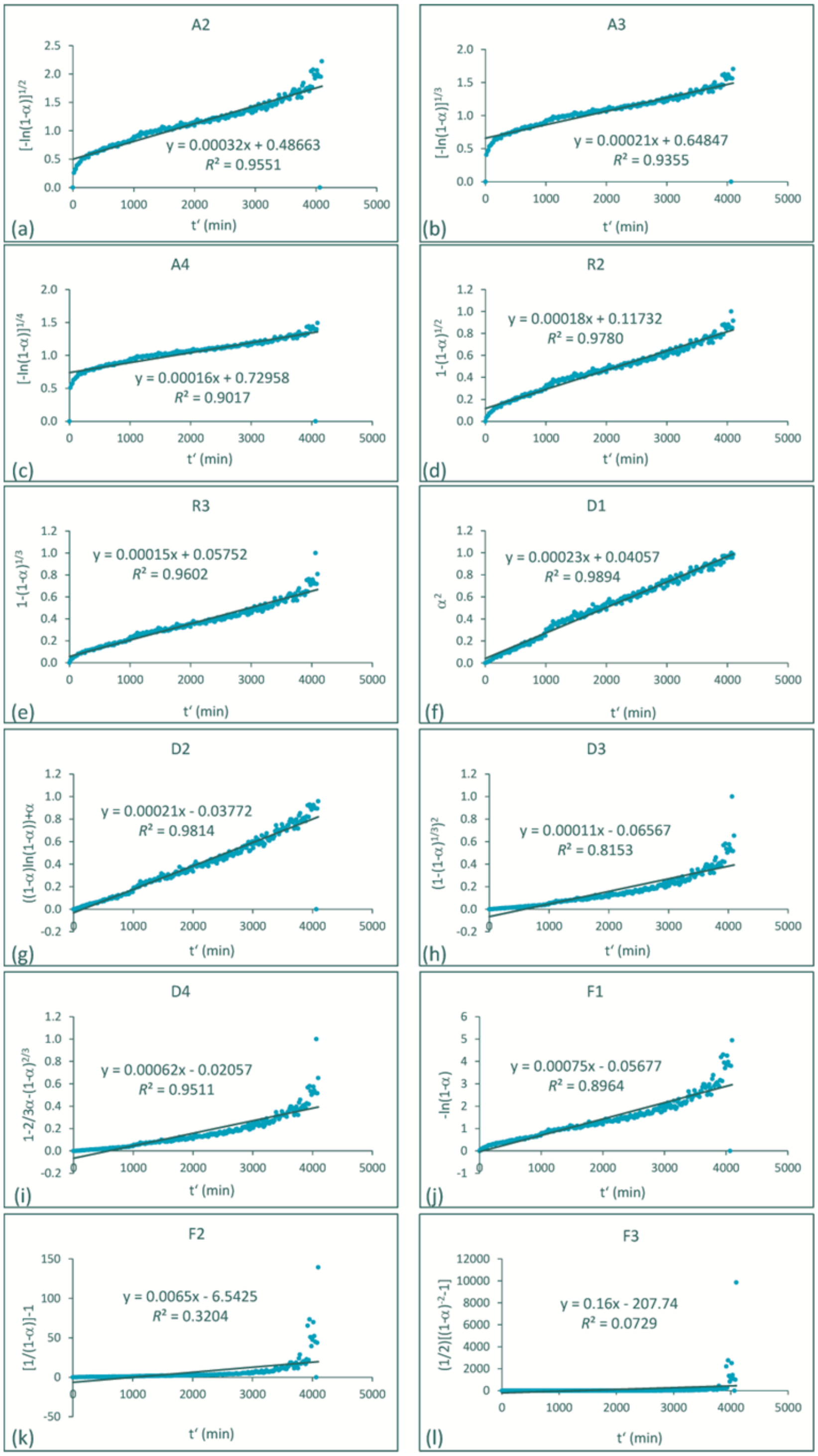

Figure S7. The fitting of conversion fraction α for the MAS *in-situ* formation of **1** (25 ℃, 10 kHz MAS, 5 μL acetonitrile**)**, after linearization α to 12 different models of solid-state reactivity: (a) the A2 model; (b) the A3 model; (c) the A4 model (d) the R2 model; (e) the R3 model; (f) the D1 model; (g) the D2 model; (h) the D3 model; (i) the D4 model; (j) the F1 model; (k) the F2 model; (l) the F3 model. The integrated rate functions $g(\alpha)$, varying for the different models, are given on the y-axis and also summarized in Table S3.

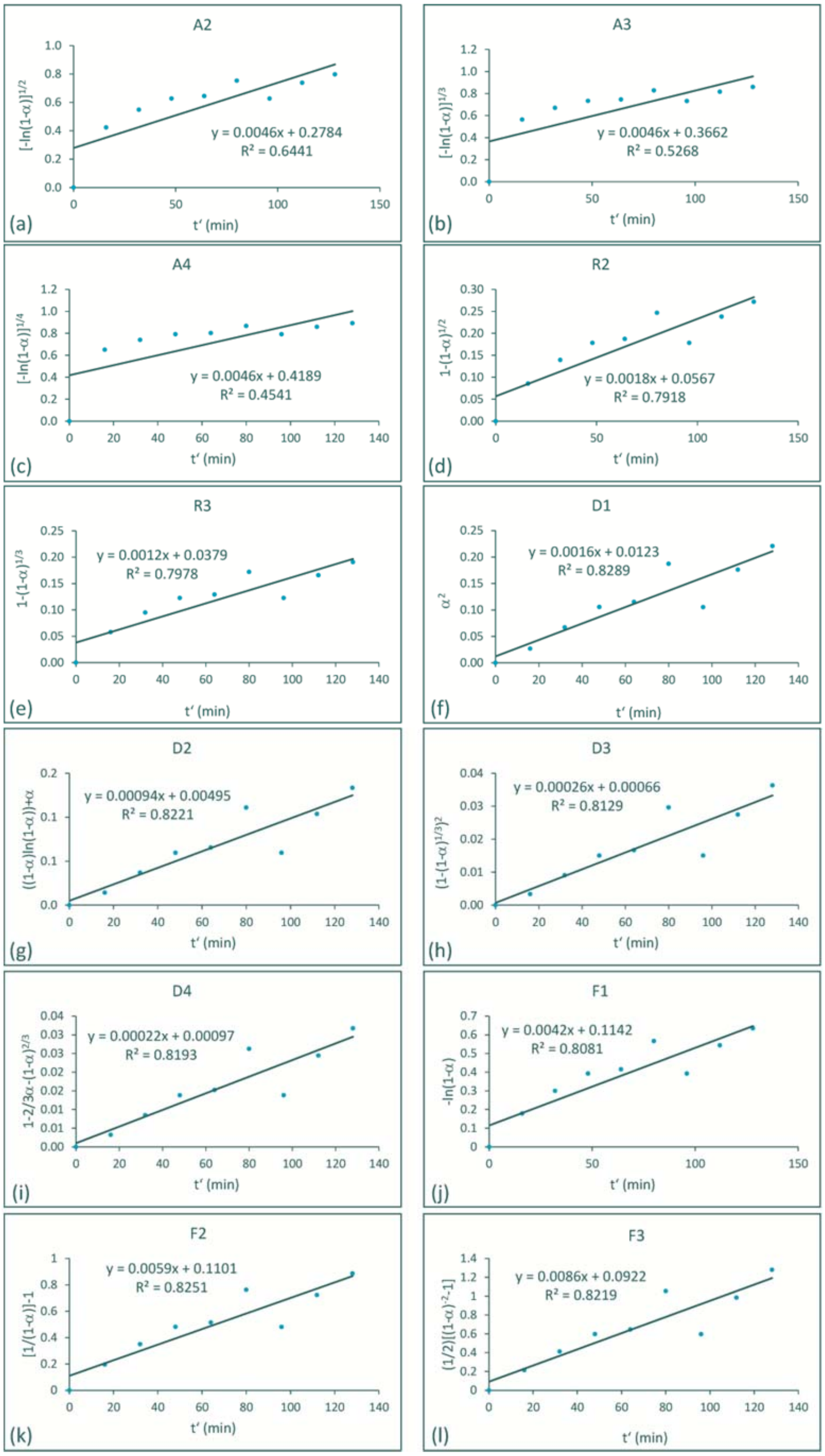

Figure S8. The fitting of conversion fraction α for the MAS *in-situ* formation of **1** (35 °C, 10 kHz MAS, 5 µL acetonitrile), after linearization α to 12 different models of solid-state reactivity: (a) the A2 model; (b) the A3 model; (c) the A4 model (d) the R2 model; (e) the R3 model; (f) the D1 model; (g) the D2 model; (h) the D3 model; (i) the D4 model; (j) the F1 model; (k) the F2 model; (l) the F3 model. The integrated rate functions $g(\alpha)$, varying for the different models, are given on the y-axis and also summarized in Table S3.

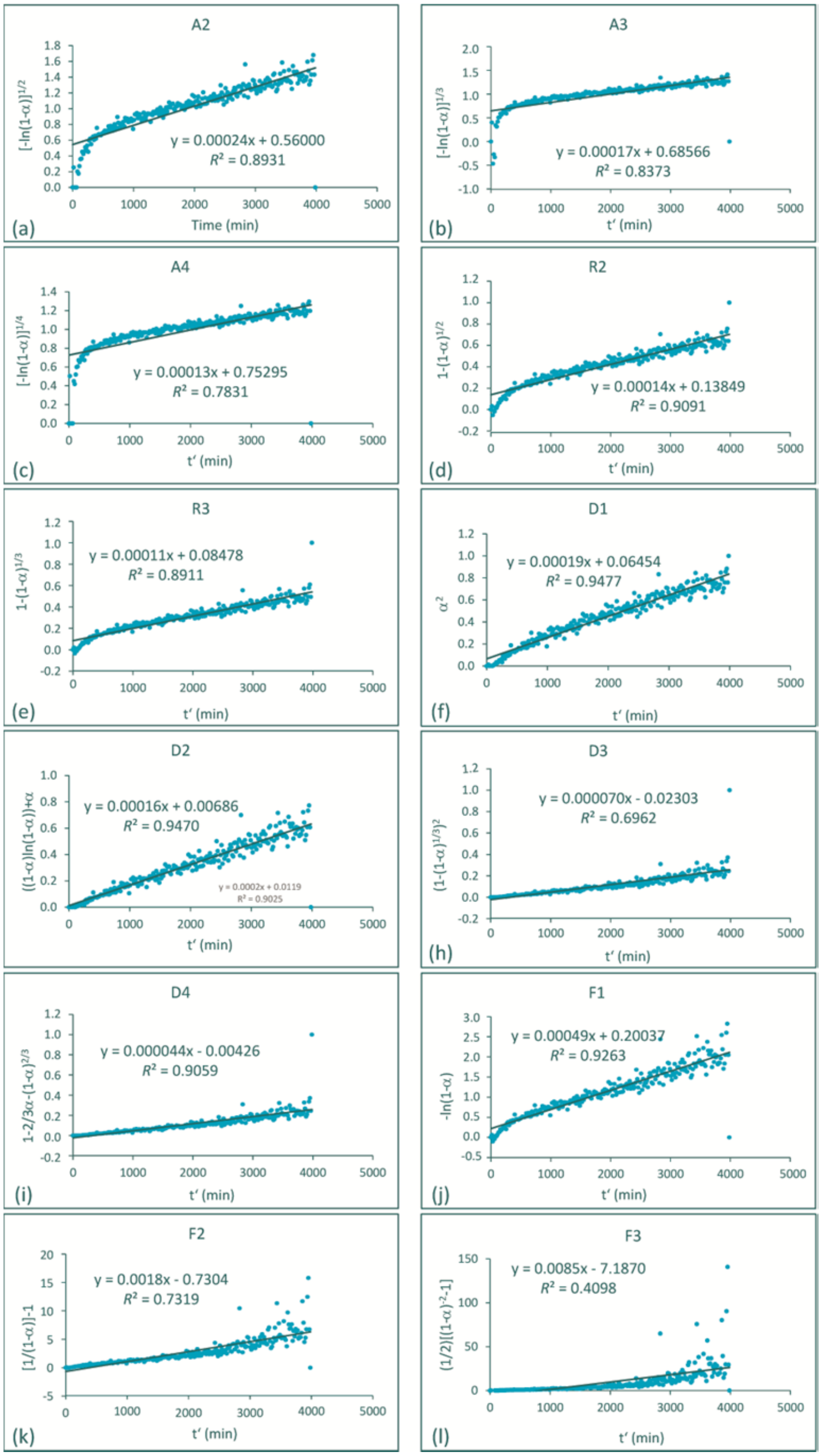

Figure S9. The fitting of conversion fraction α for the MAS *in-situ* formation of **1** (25 ℃, 8 kHz MAS, 5 μL acetonitrile), after linearization α to 12 different models of solid-state reactivity: (a) the A2 model; (b) the A3 model; (c) the A4 model (d) the R2 model; (e) the R3 model; (f) the D1 model; (g) the D2 model; (h) the D3 model; (i) the D4 model; (j) the F1 model; (k) the F2 model; (l) the F3 model. The integrated rate functions $g(\alpha)$, varying for the different models, are given on the y-axis and also summarized in Table S3.

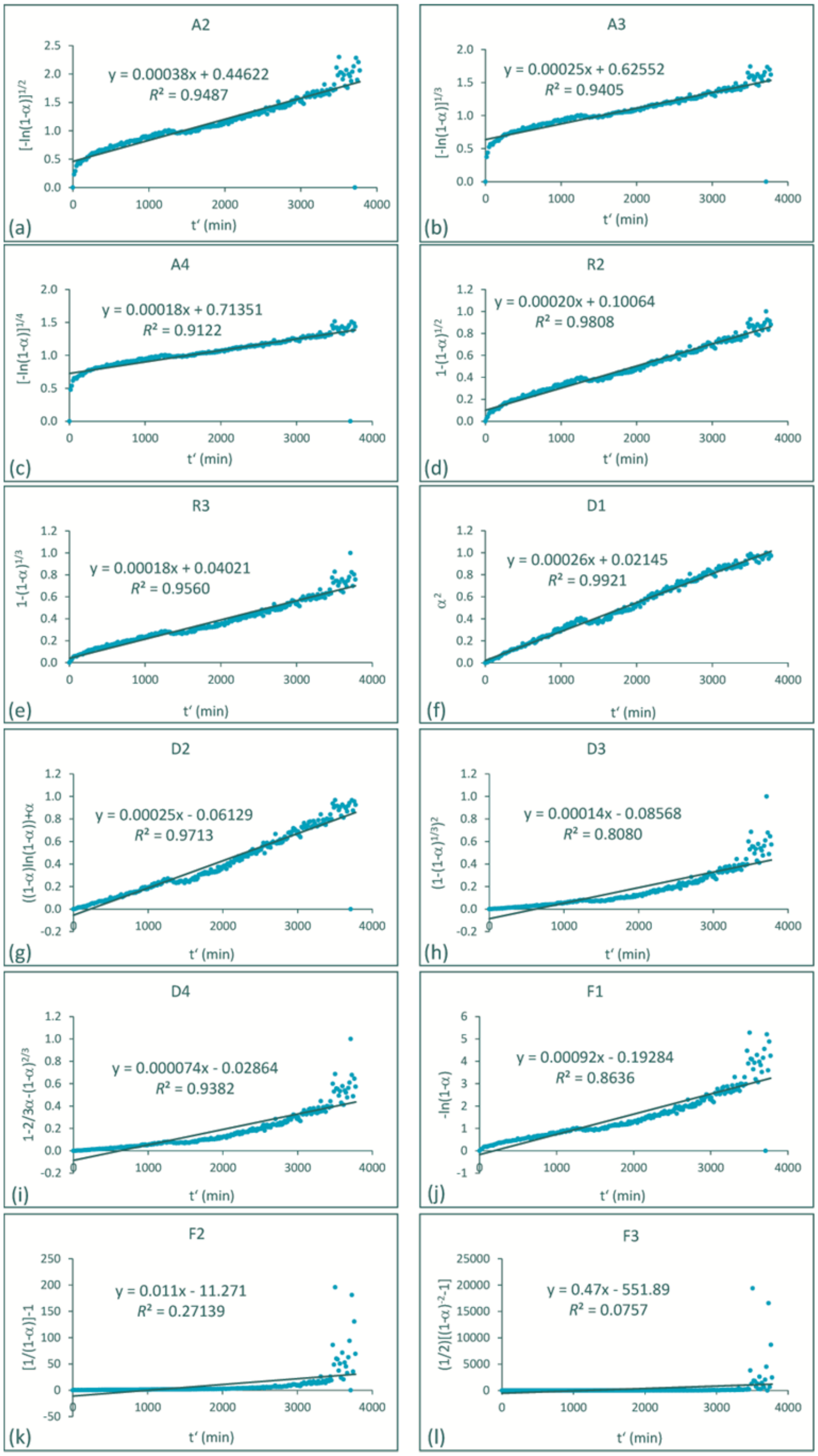

Figure S10. The fitting of conversion fraction α for the MAS *in-situ* formation of **1** (25 °C, 12 kHz MAS, 5 μL acetonitrile), after linearization α to 12 different models of solid-state reactivity: (a) the A2 model; (b) the A3 model; (c) the A4 model (d) the R2 model; (e) the R3 model; (f) the D1 model; (g) the D2 model; (h) the D3 model; (i) the D4 model; (j) the F1 model; (k) the F2 model; (l) the F3 model. The integrated rate functions, $g(\alpha)$, varying for the different models, are given on the y-axis and also summarized in Table S3.

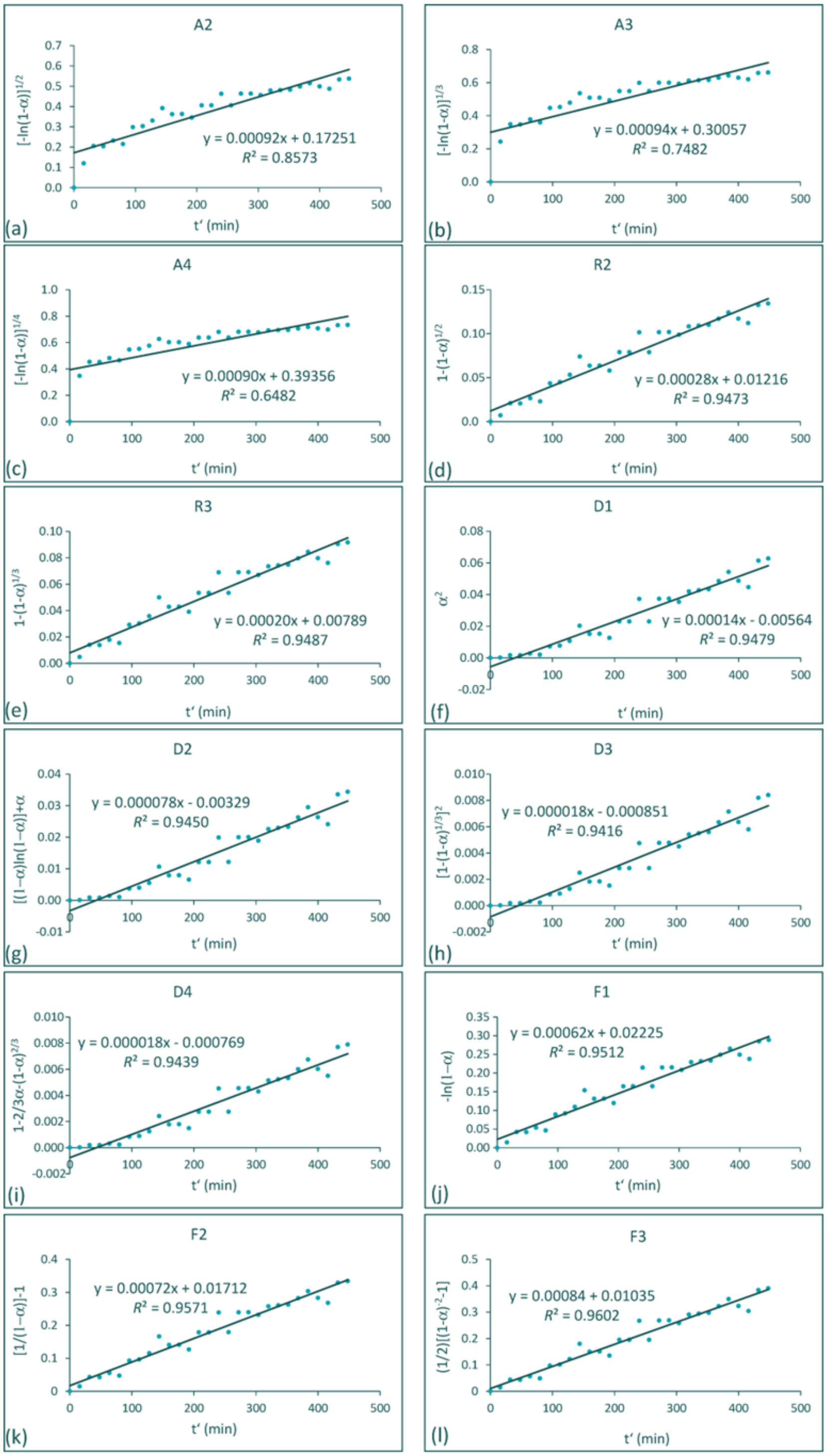

Figure S11 The fitting of conversion fraction α for the MAS *in-situ* formation of **1** (45 ℃, 10 kHz MAS, 0 μL acetonitrile), after linearization α to 12 different models of solid-state reactivity: (a) the A2 model; (b) the A3 model; (c) the A4 model (d) the R2 model; (e) the R3 model; (f) the D1 model; (g) the D2 model; (h) the D3 model; (i) the D4 model; (j) the F1 model; (k) the F2 model; (l) the F3 model. The integrated rate functions $g(\alpha)$, varying for the different models, are given on the y-axis and also summarized in Table S3.

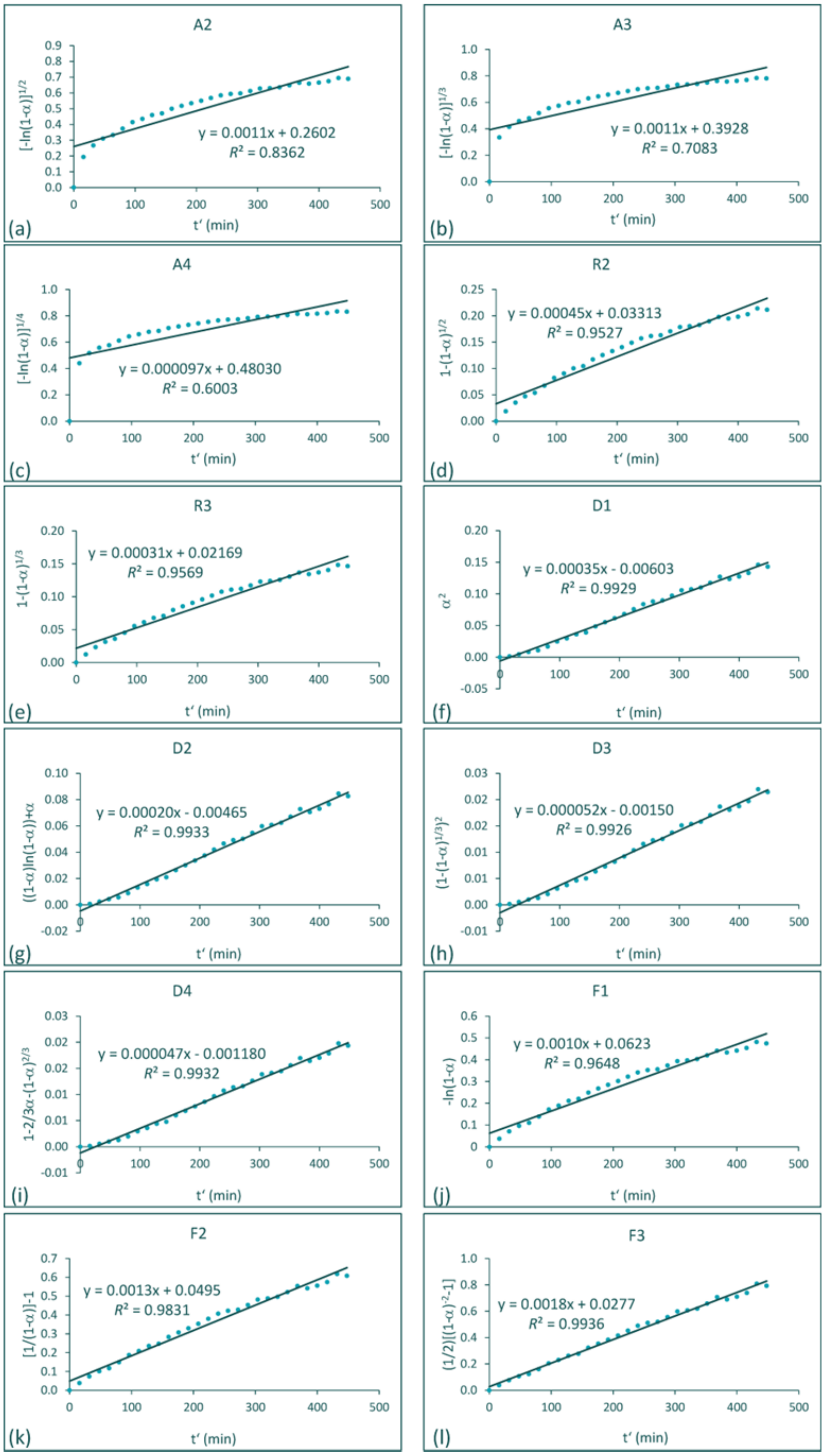

Figure S12. The fitting of conversion fraction α for the MAS *in-situ* formation of **1** (45 °C, 10 kHz MAS, 3 μL acetonitrile), after linearization α to 12 different models of solid-state reactivity: (a) the A2 model; (b) the A3 model; (c) the A4 model (d) the R2 model; (e) the R3 model; (f) the D1 model; (g) the D2 model; (h) the D3 model; (i) the D4 model; (j) the F1 model; (k) the F2 model; (l) the F3 model. The integrated rate functions $g(\alpha)$, varying for the different models, are given on the y-axis and also summarized in Table S3.

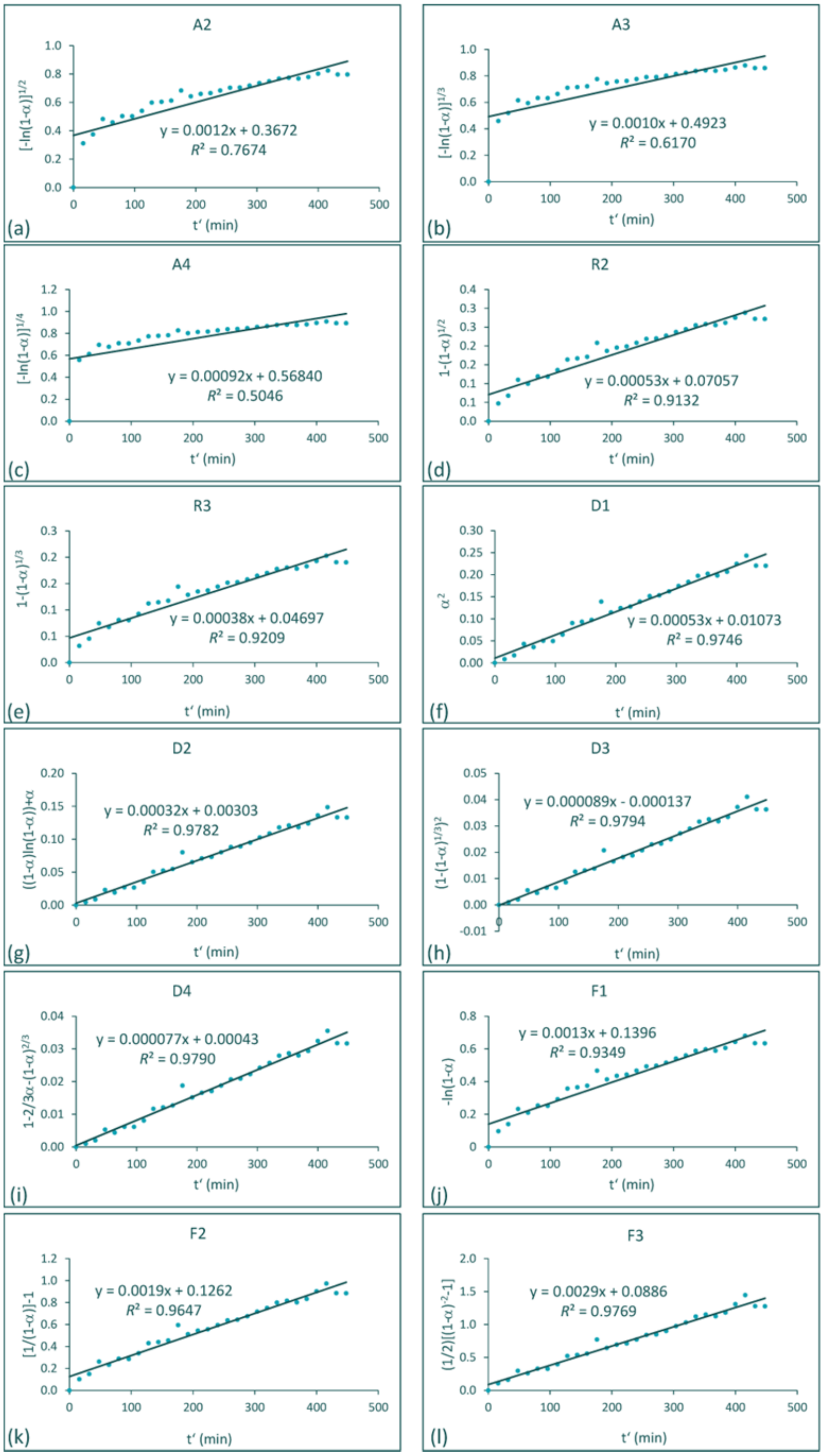

Figure S13. The fitting of conversion fraction α for the MAS *in-situ* formation of **1** (45 ℃, 10 kHz MAS, 4 μL acetonitrile), after linearization α to 12 different models of solid-state reactivity: (a) the A2 model; (b) the A3 model; (c) the A4 model (d) the R2 model; (e) the R3 model; (f) the D1 model; (g) the D2 model; (h) the D3 model; (i) the D4 model; (j) the F1 model; (k) the F2 model; (l) the F3 model. The integrated rate functions $g(\alpha)$, varying for the different models, are given on the y-axis and also summarized in Table S3.

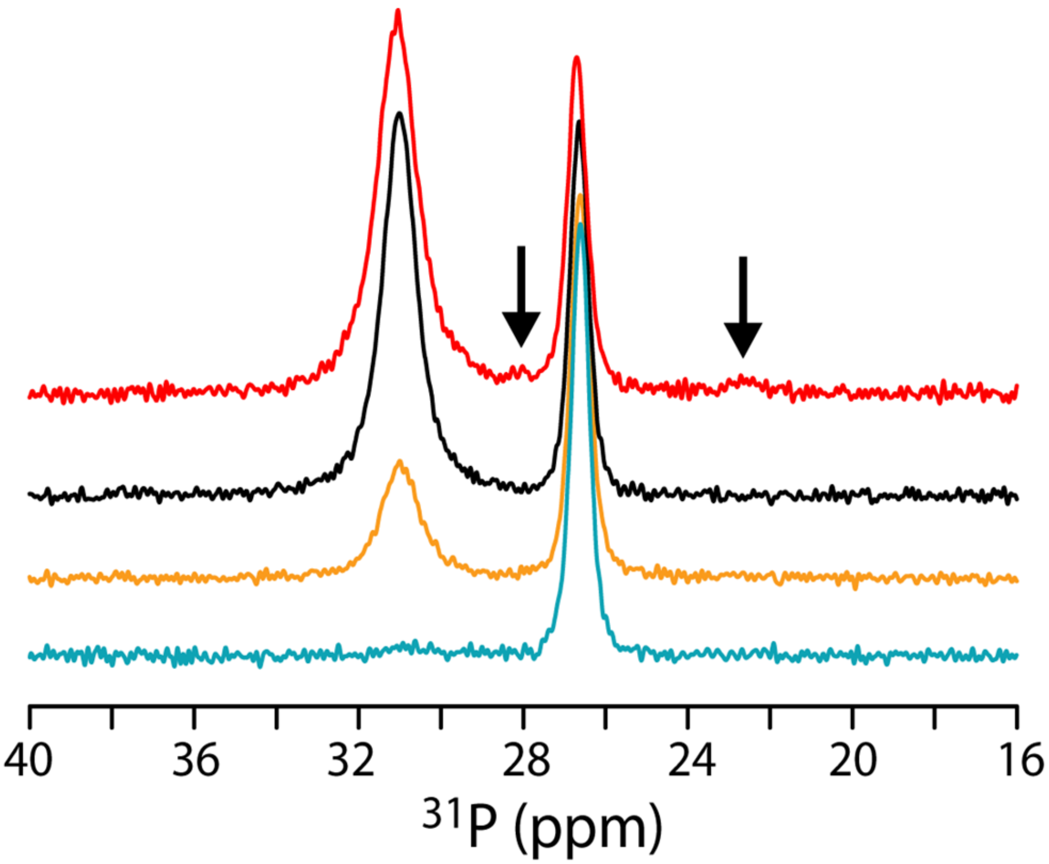

Figure S14. The *in-situ* ^{31}P CP/MAS SSNMR spectra obtained at 9.4 T at 45 °C with a 10 kHz spinning speed at $t = t_0$ after adding different initial volumes of acetonitrile: 0 µL (turquoise), 3 µL (orange), 4 µL (black), and 5 µL (red). In the last case, the arrows show the presence of a trace amount of **2**, which indicates the formation of some **2** before the first spectrum was taken.

References

1 V. S. Mandala, S. J. Loewus and M. A. Mehta, *J. Phys. Chem. Lett.*, 2014, **5**, 3340–3344.

2 G. Neue and C. Dybowski, *Solid State Nucl. Magn. Reson.*, 1997, **7**, 333–336.

3 M. D. Segall, P. J. D. Lindan, M. J. Probert, C. J. Pickard, P. J. Hasnip, S. J. Clark and M. C. Payne, *J. Phys. Condens. Matter*, 2002, **14**, 2717–2744.

4 J. P. Perdew, K. Burke and M. Ernzerhof, *Phys. Rev. Lett.*, 1996, **77**, 3865–3868.

5 C. Bonhomme, C. Gervais, F. Babonneau, C. Coelho, F. Pourpoint, T. Azaïs, S. E. Ashbrook, J. M. Griffin, J. R. Yates, F. Mauri and C. J. Pickard, *Chem. Rev.*, 2012, **112**, 5733–5779.

6 S. Adiga, D. Aebi and D. L. Bryce, *Can. J. Chem.*, 2007, **85**, 496–505.

7 2012.

8 G. M. Sheldrick, 2004.

9 G. M. Sheldrick, *Acta Crystallogr. C*, 2015, **71**, 3–8.

10 L. J. Farrugia, *J. Appl. Crystallogr.*, 1999, **32**, 837–838.

11 Y. Xu, J. Viger-Gravel, I. Korobkov and D. L. Bryce, *J. Phys. Chem. C*, 2015, **119**, 27104–27117.

12 A. Khawam and D. R. Flanagan, *J. Phys. Chem. B*, 2006, **110**, 17315–17328.

13 J. D. Hancock and J. H. Sharp, *J. Am. Ceram. Soc.*, 1972, **55**, 74–77.